

The thermal conductivity of “pastas” in neutron star matter

C.O. Dorso

*Departamento de Física, Facultad de Ciencias Exactas y Naturales, Universidad de Buenos Aires,
Pabellón I, Ciudad Universitaria, 1428 Buenos Aires, Argentina. and
Instituto de Física de Buenos Aires, Pabellón I,
Ciudad Universitaria, 1428 Buenos Aires, Argentina.**

Jonathan Dunn and Alejandro Strachan

*School of Materials Engineering, Purdue University, Neil Armstrong Hall of Engineering,
701 West Stadium Avenue, West Lafayette, Indiana, 47907, USA.*

G.A. Frank

*Unidad de Investigación y Desarrollo de las Ingenierías,
Universidad Tecnológica Nacional, Facultad Regional Buenos Aires,
Av. Medrano 951, 1179 Buenos Aires, Argentina.*

(Dated: May 20, 2020)

This investigation explores the phononic thermal conductivity of nuclear star matter as it undergoes the “topological” transition to the “pasta” regime, and further down to the solid-liquid phase transition. The study was carried out using molecular dynamics simulations with nuclear potentials embedded in an effective (*i.e.* Thomas-Fermi) Coulomb potential. The thermal conductivity experiences a dramatic change within a narrow temperature interval around $T \simeq 1$ MeV. This change accomplishes the “pasta” breakdown during a heating process. The thermal conductivity by flipping protons’ or neutrons’ velocity further shows a decoupling for asymmetric nuclear star matter.

I. INTRODUCTION

Neutron stars are expected to exist at temperatures as high as $T \sim 9$ MeV, although a fast cooling process takes place soon after their birth. This process is caused by neutrino emission and determines the structural evolution of the star (see Ref. [1] for an insight on the associated neutrino opacity). The thermal conductivity, κ , and viscosity, η , of neutron star matter (NSM) are hypothesized to determine the state of the star (specially, its crust) [2].

The crust exhibits nucleon densities from 10^{-11} fm^{-3} to 0.1 fm^{-3} [3, 4], and its inner region (beyond 10^{-4} fm^{-3}) exhibits complex structural transformations, depending on the nucleon density. Lower densities result in nuclei embedded in an electron and neutron gas. Densities above $\rho \sim 0.01 \text{ fm}^{-3}$, however, may lead to complex structures, denoted *pastas* [4–8].

The thermal conductivity across the “inner crust” is expected to be sensitive to temperature and the fraction of species [7, 8]. Although it was first accepted for the protons and neutrons conductivity (κ_p and κ_n , respectively) to be negligible with respect to that of electrons [2], researchers pointed out that κ_p and κ_n can actually influence the thermal relaxation of a neutron star [3, 7–10].

Clearly κ_n becomes increasingly relevant as the neutron star matter becomes neutron-rich [2]. In addition, other phenomena, such as strong magnetic fields, may reduce the electrons’ contribution [7], enhancing not only the κ_n contribution but also the κ_p contribution. The later has been shown to produce considerable reduction of kinetic coefficients, even at small proton concentrations (*i.e.* β -stable matter) [10].

The effect of nucleon thermal conductivity on the late-time cooling of neutron stars is somewhat controversial throughout the literature. The observed late-time cooling of neutron stars (e.g., MXB 1659-29) was shown to be consistent with low thermal conductivities [11]. However, the existence of “impurities” in the *pasta* environment had to be postulated in order to match the right cooling curve [8]. Also, the finding of “spiral defects” within this context was considered as an additional source of electron scattering [11, 12].

Regardless of the existence of defects in the *pasta* environment, the true “effective” conductivity remains rather uncertain. Variations of an order of magnitude may be expected due to the alignment of the *pasta* structures with respect to the radial axis of the star [8]. Randomly oriented “*pasta* slabs” may reduce the conductivity by 37%, according to molecular dynamics simulations reported in Ref. [8].

Some criticism on these conductivity estimates arose in recent years. Researchers observe that the use of different potentials may lead to variations of one order of magnitude of the nucleon contribution to transport

* codorso@df.uba.ar

coefficients [13]. The formalism of the “impurity” parameters has also been questioned, arguing the lack of meaning of (high) impurity fractions out of the context of uniform crystals [14]. Current simulations, however, are not able to predict more convincing κ values for matching the late cooling of MXB1659-29 [14]. Other phenomena, related to the electrical conductivities, may also fail to explain the absence of X-ray pulsars with periods larger than 12 s [14].

Our concern is placed on the “inner” crust situation at low to moderate temperatures. The *pasta* phase is expected to dominate the topological scene at the sub-saturation densities [5, 15]. This topological regime has already been studied in the context of the equation of state (EoS) [5, 15, 16]. But research on the thermal conductivity still focuses on the energy carried by electrons, disregarding the energy flux due to collisions between nuclear species [7, 8, 14]. Other research areas have insisted on the role of the non-electronic heat carriers in lattice-like or liquid-like systems [17, 18].

We will focus on the heat conduction due to nucleons in the *pasta* regime. We presume that topological structures may enhance or hinder the energy transport due to nuclear carriers, as first observed in Ref. [19]. We will consider, however, that nucleons are embedded in an electron gas environment, in order to accomplish a charge-neutral system of nucleons and electrons. The term “thermal conductivity” in this context means the “phononic” or “lattice” contribution to the thermal conductivity. No further mention to the electron contribution will be done.

The paper is organized as follows. Section II summarizes the theoretical background for the thermal conductivity κ in the context of the molecular dynamics model (MD). Section III explains the preparations for measuring κ within the *pasta* scenario. The corresponding results are exhibited in Section IV. For clarity reasons, we separated the analysis into symmetric and non-symmetric matter. Our conclusions are presented in Section V.

II. BACKGROUND

We use classical molecular dynamics (CMD) to characterize the thermal transport of nuclear star matter. This approach naturally drives the system to its free energy minima within a very complex energy landscape given by the inter-particle interactions and boundary conditions. Literature results on the validity of this approach can be found in Refs. [5, 6, 15, 20, 21].

Parameter	Value	Units
V_r	3097.0	MeV
V_a	2696.0	MeV
V_0	379.5	MeV
μ_r	1.648	fm ⁻¹
μ_a	1.528	fm ⁻¹
μ_0	1.628	fm ⁻¹
λ	10	fm
r_c	5.4	fm
r'_c	20	fm

TABLE I. Parameter set for the CMD computations (New Medium model).

A. The potentials

Nuclear matter is considered as a three particle system composed of protons, neutrons and electrons. The latter, however, is envisaged as a gas that actually introduces a screening effect on the Coulomb potential between protons. The potentials for neutron-proton (np), neutron-neutron (nn) and proton-proton (pp) interactions were first set by Pandharipande to attain a binding energy at the saturation density of 250 MeV. The electrons screening effect was later introduced through a Thomas-Fermi potential with an “effective” screening length λ of 20 fm [22]. The whole set reads as follows

$$\begin{aligned}
 V_{np}(r) &= \frac{V_r}{r} e^{-\mu_r r} - \frac{V_r}{r_c} e^{-\mu_r r_c} - \frac{V_a}{r} e^{-\mu_a r} + \frac{V_a}{r_c} e^{-\mu_a r_c} \\
 V_{nn}(r) &= \frac{V_0}{r} e^{-\mu_0 r} - \frac{V_0}{r_c} e^{-\mu_0 r_c} \\
 V_{pp}(r) &= V_{nn}(r) + \frac{q^2}{r} e^{-r/\lambda} - \frac{q^2}{r'_c} e^{-r'_c/\lambda}
 \end{aligned} \tag{1}$$

where q is the electron charge and r_c, r'_c are the cutoff distances for the Pandharipande and Thomas-Fermi potentials, respectively. The value for the parameters appearing in Eq. 1 can be seen in Table I.

B. The thermal conductivity

The thermal conductivity κ corresponds to the set of transport coefficients relating the heat flux (*i.e.* energy flux \mathbf{J}) to the temperature gradient ∇T , through the (phenomenological) Fourier law

$$\mathbf{J}(t) = -\kappa \nabla T \tag{2}$$

where κ corresponds to a second rank 3×3 tensor for non-isotropic matter. Notice that the constitu-

tive relation (2) is intended as a “macroscopic” one, whenever matter is considered as a continuum. The energy flux \mathbf{J} represents a somewhat “mean” flux density $\langle \mathbf{j} \rangle$ transported across a small volume \mathcal{V} (that is, $\mathbf{J} = \langle \mathbf{j} \rangle \cdot \mathcal{V}$). The calculation of thermal transport properties from atomistic simulations is well established.[23–26]

We will only consider those situations where \mathbf{J} and ∇T are collinear (say, for example, along the \hat{z} axis) and use a non-equilibrium method for computing the thermal conductivity κ_z is proposed by Müller-Plathe (see Ref. [23]) from the average heat flux and temperature gradient.

$$\kappa_z = - \lim_{t \rightarrow \infty} \frac{\langle J_z \rangle}{\langle \partial T / \partial z \rangle} \quad (3)$$

If the medium is isotropic, common practice sets the mean thermal conductivity as $(k_x + k_y + k_z)/3$.

Notice that the linear nature of Eqs. (2) and (3) requires relatively small temperature gradients.

In a nutshell, the Müller-Plathe procedure [23] generates a heat flux of known magnitude and the temperature gradient is obtained as local averages of the kinetic energy. The system is divided in thin bins along the the heat flux direction (see Fig. 1 for details); the first slab is labeled as the “cold” slab, while the slab in the middle is labeled as “hot”. A heat flux is generated by exchanging the velocities of two particles (with the same mass), the hottest particle in the “cold” bin and the coldest one in the “hot” bin (see Fig. 1). Thus, the system is (artificially) driven out of equilibrium, and a heat flux \mathbf{J} develops through the system of interest in the opposite direction for the equilibrium restoration. This flux is expected to reach the stationary state if the exchanging rate is held regularly for a long time.

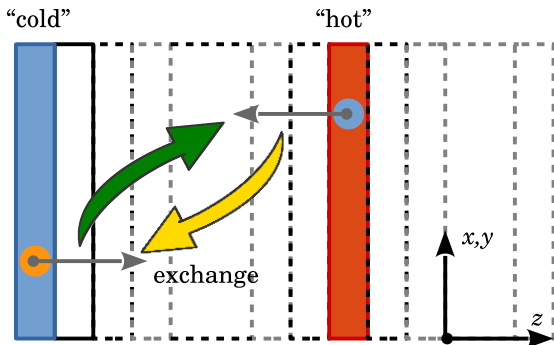


FIG. 1. (On-line color only) Schematic representation of the Müller-Plathe procedure. The blue and red bins correspond to the “cold” and “hot” slabs, respectively. The horizontal flat arrows stand for the particles velocity. The curved arrows (green and yellow, respectively) represent the velocity exchange process.

In order to generate an external heat flux, particle velocity exchanges are performed periodically during the MD simulation. Recall that the species themselves are not exchanged, but only the velocities. Thus, the “pumping” process only transports kinetic energy (for particles with the same mass). This procedure conserves total energy and linear momentum.

The heat flux introduced by the velocity exchange is hard to compute from dynamical magnitudes. The computation from the net transported (kinetic) energy is somewhat easier since

$$\langle J_z \rangle + \frac{1}{2A_{xy}} \left[\frac{1}{\tau} \sum_{n=1}^T \frac{1}{2} m (v_h^2 - v_c^2) \right] = 0 \quad (4)$$

where the expression between the square brackets represents the mean (kinetic) energy exchanged during the time period τ . v_h and v_c refers to the velocities of the hot particle and cold particle, respectively. The factor $2A_{xy}$ corresponds to the cross section of the slabs (two faces).

The temperature profile is obtained by computing the local (kinetic) temperature for each slab. Once steady state is reached, the temperature profile is expected to be linear away from the cold and hot bins where velocities are exchanged, provided the heat flux remains small. Further details can be found in Ref. [23].

We stress the fact that the balance condition (4) links the heat flux \mathbf{J} to the (artificial) kinetic energy transportation introduced by the Müller-Plathe procedure. The velocity exchange is not restricted to pairs of similar particles, but also across species (with the same mass). Therefore, the procedure enables the computation of the thermal conductivity for the set of *all* the nucleons, or for the set of protons and neutrons separately. The meaning of either coefficients, though, will be quite different.

III. SIMULATIONS

The MD simulations were performed using the Verlet integration scheme (with periodic boundary conditions). The Nosé-Hoover thermostat was used to drive the system to the desired temperature with a coupling constant of 10 (time units). All simulations were performed with the LAMMPS simulation code running on GPU’s (Graphic Processing Units) [27].

We were able to simulate around 100,000 nucleons in the primary cubic cell. However, the *pasta* topology became so complex that the resulting thermal conductivity represented that of a complex structure. Thus, we

restricted our study to the most elementary topologies (say, straight *lasagnas* or *spaghettis*) accomplished by a system size of 4,000 nucleons.

At a first instance, the system was cooled from $T = 4$ MeV down to the solid (pasta) state (say, $T = 0.1$ MeV). The density ρ ranged from 0.03 fm^{-3} to 0.05 fm^{-3} . Nice *lasagnas* or *spaghettis* resulted after the cooling, although not completely aligned to the canonical axes (see below). In order to improve the alignment, we softened the *pasta* by raising the bath temperature to $0.8 - 1.2$ MeV, and then, we performed the corresponding transformations. The *pasta* was finally cooled back to 0.1 MeV.

At a second instance, the bath temperature was increases from 0.1 MeV to 2.1 MeV, while the nucleons' positions and velocities were recorded at regular time intervals. The recorded configurations were set as the initial conditions for the thermal conductivity measurements.

The thermal conductivities reported in Section IV correspond to those obtained following the Müller-Plathe procedure (see Ref. [23]). Data was collected after a steady state was reached from each initial condition (within the fluctuations typical of small systems). Recall that the Müller-Plathe procedure is known to attain a precision of 10% (on a system of 2600 Lennard-Jones particles [23]).

The Müller-Plathe procedure requires the binning of the primary cell, in order to compute the temperature gradient across the bins (that is, along the heating flux direction). This is why we demanded a proper alignment of the *pasta* with respect to the canonical axes. We set the number of bins to 20.

For each pasta topology we computed two values of the thermal conductivity: “parallel” and “transverse”. The former corresponds to the heat flux along the *pasta*. The latter corresponds to the heat flux running across the *pasta*. Each measurement were computed separately.

Whatever the heat flux direction, we computed the thermal conductivity by either flipping the protons' and neutrons' velocity separately, and *all* the nucleons regardless of their nature. The former means that only one specie contributes to the velocity exchange in Eq. (4). This distinction became very useful when analyzing non-symmetric matter (see Section IV B).

We made a preliminary check of our result with the few data reported in literature [19]. Fig. 2 shows our output for an 1:1:1 simulation cell and the reported data for larger cells. The thermal conductivity was computed over *all* the nucleons arranged in a *lasagna*-like topology.

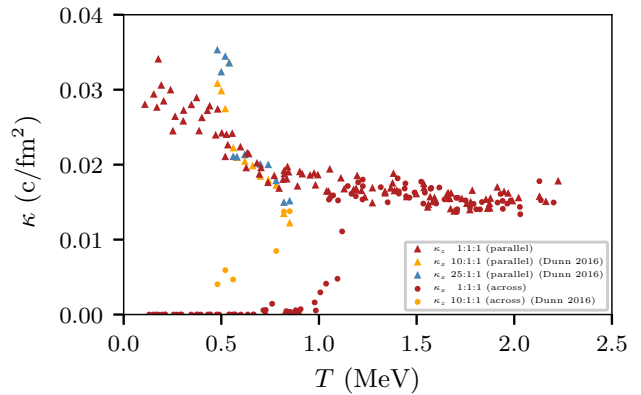


FIG. 2. (On-line color only) Thermal conductivity κ vs. temperature. The red symbols correspond to our simulations during the heating evolution after the *lasagna* was established. The orange and blue symbols correspond to literature data. All data points correspond to a system density of $\rho = 0.05$ ($x = 0.5$) and computations were done on *all* the nucleons. The aspect ratio of simulation cells is indicated in the insert.

Notice from Fig. 2 that our preliminary results match the ones reported in Ref. [19] for the “parallel” measurement (triangular symbols in Fig. 2). Our “across” measurements, however, do not completely agree with Ref. [19]. But since the number of slabs (and the space binning) in Ref. [19] may be different from ours, no definite conclusions can be drawn about the mismatch. Nevertheless, both data sets exhibit a similar qualitative behavior. Recall that our objective is understanding the influence of *pasta* structures on the energy transport.

IV. RESULTS

A. Symmetric matter

1. The caloric curve

As mentioned in Section III, we focused on relatively small cells housing 4,000 nucleons (with periodic boundary conditions). The simulation cell was previously cooled according to the protocol detailed in Section III. Fig 3 (orange line) shows the energy (per nucleon) during heating following this initial annealing.

The Müller-Plathe procedure introduces a periodical velocity exchange between nucleons, as explained in Section II B. This kind of energy exchange induces a heat flux across the cell, while the corresponding temperature gradient appears along the same flux direction. This results in a perturbed system due to this (externally) induced heat flux. Fig 3 shows the internal energy (per nucleon) when the heat flux is

parallel (red line) and transverse (blue line) to the *lasagna*. Comparisons can be made with respect to the energy of the unperturbed system. The inserted snapshots correspond to the protons' distribution after a parallel heat flux was established (see caption for details).

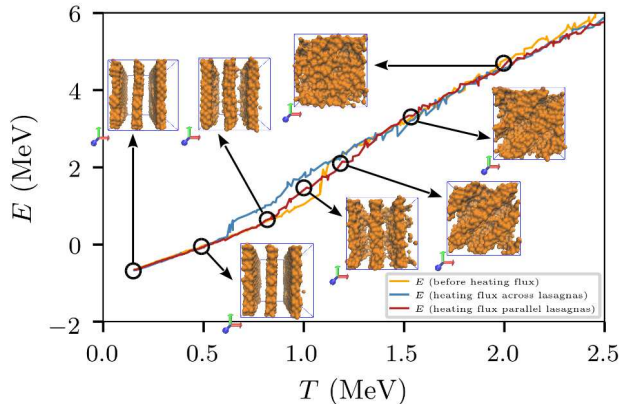


FIG. 3. (On-line color only) Internal energy vs. temperature during the heating evolution after a *lasagna* was established. The system density was $\rho = 0.05$ and the proton ratio was $x = 0.5$. The surface plots show only the protons' topology. Three situations are represented: (a) The energy evolution just before a heat flux was induced (orange line). (b) The energy evolution after the a heat flux was established across the *lasagnas* (blue line). (c) The energy evolution after the a heat flux was established parallel to the *lasagnas* (red line).

The internal energy prior to any measurement perturbation (say, before introducing a heat flux in a specific direction) exhibits a sharp “jump” at $T \simeq 1.25$ MeV (see orange line in Fig. 3). This jump corresponds to the “pasta” breakdown (*i.e.* the topological transition [15]). Interestingly, Fig. 3 also shows that the energy-temperature relationship changes when a heat flux (and a temperature gradient) is introduced, using the Müller-Plathe procedure in our case. The snapshots in Fig. 3 capture the relation, at least qualitative, that exists between the energy profile and the changes in the system topology.

A comparison between the internal energy curve of *spaghettis* and *lasagnas* can be performed from Fig. 4. Notice that both curves are essentially the same, although the *lasagna* profile appears shifted upward with respect to the *spaghetti* one. The energy “jump” is also present near $T \simeq 1.25$ MeV for the *spaghettis*, achieving the corresponding topological breakdown. The Müller-Plathe perturbation can further be seen.

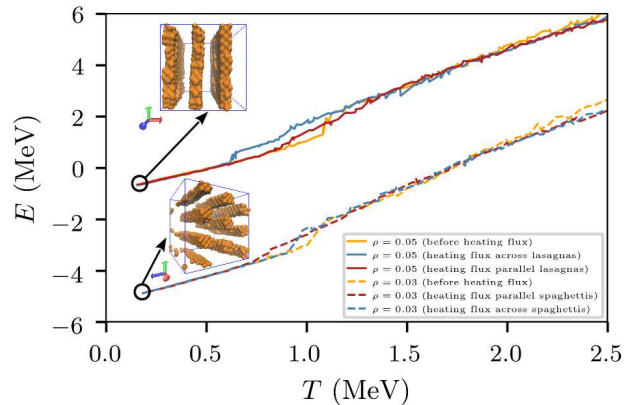


FIG. 4. (On-line color only) Internal energy vs. temperature during the heating evolution after the *pasta* was established. Two different pastas are represented: a spaghetti-like system ($\rho = 0.03$ and $x = 0.5$), and a lasagna-like system ($\rho = 0.05$ and $x = 0.5$). The former corresponds to the dashed lines, while the later corresponds to the continuous lines.

2. The thermal conductivity κ

We first computed the thermal conductivity for symmetric neutron star matter ($x = 0.5$) as a function of temperature in the 0.1 – 2.1 MeV range. This includes the solid-liquid transition ($T \sim 0.5$ MeV) and the topological transition ($T \sim 1$ MeV). The computation was carried out in two ways: by considering the heat flux due to *all* the nucleons, or, considering only *one* kind on nucleons (say, the protons; see Section III for details). Fig. 5a shows the proton thermal conductivity for a wide temperature range. Fig. 5b shows the details of the smoothed data computations obtained for either protons and *all* the nucleons.

Two regimes can be distinguished immediately according to Fig. 5. The thermal conductivity exhibits a smooth slope above $T \simeq 1.25$ MeV, while a dramatic change occurs below this threshold. The later appears as a “decoupling” between the thermal conductivity parallel to the *lasagna* (κ_z) and the one orthogonal to this direction (κ_x). The “decoupling” pattern is essentially the same whether all the nucleons are considered or only the protons (for $x = 0.5$).

It can be noticed in Fig. 5 that the conductivity for *all* the nucleons appears somewhat shifted up with respect to the protons' conductivity. The large fluctuations in the data do not allow a definite conclusion on this phenomenon. However, a small bias seems reasonable due the (local) density of the considered specie (say, nucleons or protons only). An insight to this issue is given at the end of this Section.

We turn to study the topology of the nucleons in

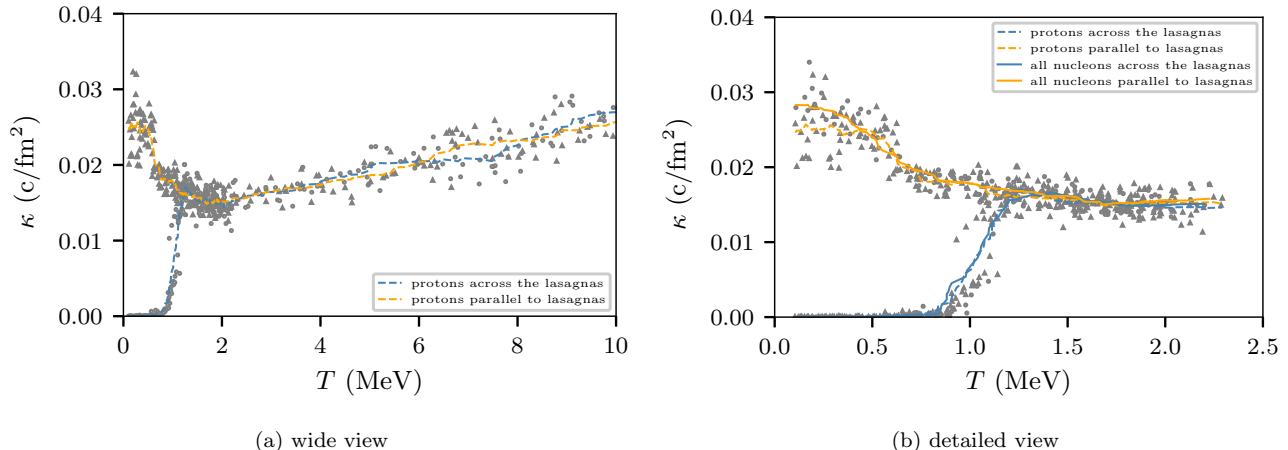


FIG. 5. (On-line color only) Thermal conductivity κ vs. temperature during the heating evolution after the *lasagna* was established (see Fig. 3 for the corresponding snapshots). The system density was $\rho = 0.05$ ($x = 0.5$). The smoothing was done following a moving average procedure of ± 10 points. The rounded gray points correspond to the raw data obtained over *all* the nucleons. The triangular gray points correspond to the raw data obtained over *protons* only.

the simulation cell for a better understanding of the “decoupling threshold”. We measured the number of clusters (of the 4000 nucleons) within the simulation cell. Only the particles in the cell were taken into account while performing the cluster analysis (no images included). In fact, the *lasagnas* are infinite in, say the (x, y) plane, but the system is discontinuous in the \hat{z} direction. Fig. 6 shows the results for the evolution in Fig. 3. The cut-off distance between neighbors belonging to the same cluster was set to $r_c = 4$ fm, in order to get exactly three clusters at $T = 0.1$ MeV (see Fig. 3).

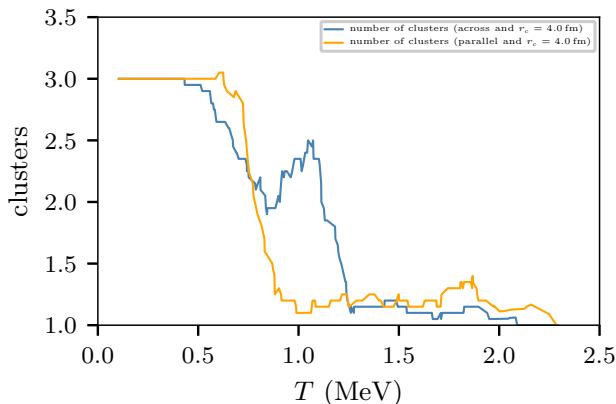


FIG. 6. (On-line color only) Number of clusters in the simulation cell for the *lasagna*-like structures shown in Fig. 3. Data corresponds to two heat flux: parallel or across the *lasagna* structure (see insert for details). The smoothing was done following a moving average procedure of ± 10 points. The cut-off distance was set to 4 fm.

According to Fig. 6, the number of clusters drops off

near $T = 1$ MeV. This corresponds to the *lasagna* breakdown shown in Fig. 3. The fluctuations observed at the drop off interval (say, 1 – 1.25 MeV) correspond to weak (or temporary) connections between slabs during the evolution. These can be noticed in Fig. 5 by watching the raw data points, although its trace is lost after the smoothing procedure. The “decoupling” threshold is thus associated to this enhanced connectivity among nucleons (meaning the pasta breakdown).

The vanishing values of the thermal conductivity across a well established *lasagna* (say, for $T < 1$ MeV) can be easily explained because of the existence of voids between the slabs. The negative slope for the parallel κ (*i.e.* along the *lasagna*) means that the “solid pasta” presents an enhanced conductivity with respect to the “liquid pasta”. This behavior is common to other materials.

The slab structure of the *lasagnas* undergoes openings for decreasing densities in the simulation cell. Fig. 7 shows how these openings spread over the slabs until the *lasagna* is no longer sustainable, moving to the *spaghetti*-like structure (see Fig. 7a). Fig. 8 exhibits the corresponding proton thermal conductivity (after the data smoothing).

The “decoupling” pattern goes through the explored densities (see Fig. 8), including either *spaghettis* or *lasagnas*. The “decoupling threshold” (say, $T \simeq 1.25$ MeV) remains unchanged (within the current measurement errors). The (parallel) thermal conductivity, however, exhibits a density dependency on either side of this threshold. According to Fig. 8, the parallel κ (protons only) increases for increasing densities all along the explored temperatures. The orthogonal κ (protons only)

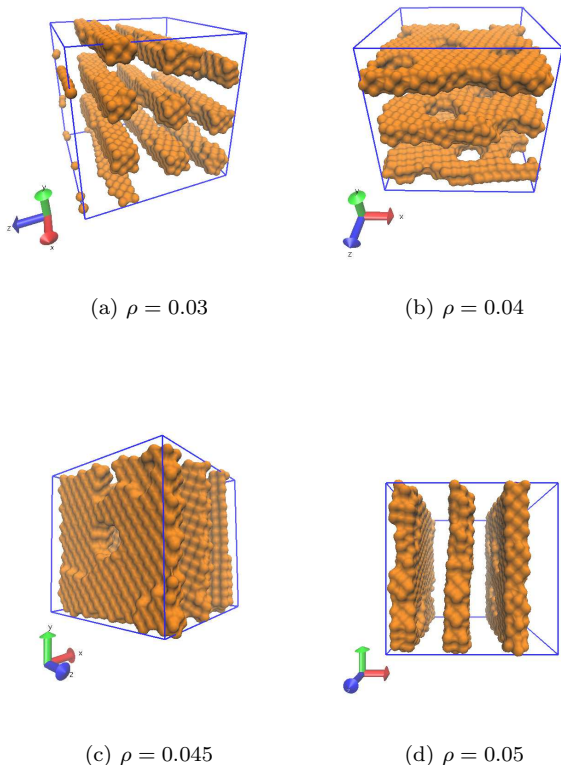


FIG. 7. Surface plots for protons at $T = 0.1$ MeV ($x = 0.5$). The nucleon densities are indicated below each snapshot.

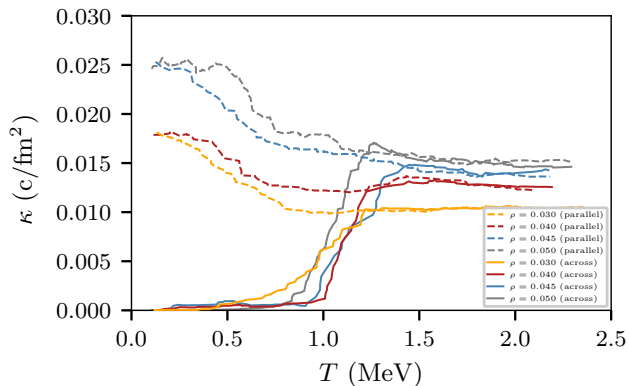


FIG. 8. (On-line color only) Proton thermal conductivity κ vs. temperature for densities in the range 0.03 to 0.05 fm^{-3} and $x = 0.5$ (see insert for details). The smoothing was done following a moving average procedure of ± 10 points. The dashed lines correspond to the thermal conductivity values along (parallel) the pasta structure. The continuous lines correspond to the thermal conductivity across the pasta structure.

meet this behavior above the “decoupling threshold”, that is, after the pasta breakdown occurs.

Notice that the solid-like state also attains some kind of density dependence for κ (protons only). The current fluctuations of our measurements does not allow to distinguish clearly between the corresponding thermal conductivity values at $\rho = 0.03$ (*spaghettis*) and $\rho = 0.04$ (washed out *lasagna*). But Fig. 8 shows fairly different values between $\rho = 0.03$ and $\rho = 0.05$.

We may summarize our results as follows. The *pasta* breakdown process (during a heating evolution) accomplishes a dramatic change in the thermal conductivity of symmetric neutron star matter. For “cold” *pastas*, the thermal conductivity is only possible along the *pasta* structure, attaining a “decoupling” between orthogonal directions. The solid state of “cold” *pastas* even enhances the conductivity. But warming the *pastas* above the threshold $T \simeq 1.25$ MeV, breaks down its topological structure, connecting regions that were once separated by voids. This situation allows heating on any direction, and thus, the thermal conductivity switches to an homogeneous (isotropic) value, that may depend on the system density.

B. Non-symmetric matter

The next step in the investigation focused on the thermal conductivity behavior for proton ratios varying from $x = 0.5$ down to $x = 0.3$. The nucleons’ potentials remained unchanged, as expressed in Section 1. Fig. 9 shows the corresponding profiles (up-to the cut-off distance) in comparison with a *lasagna*-like background. Notice that the slabs widths do not exceed the cut-off distance, although they look more irregular than in the case of symmetric matter. For the sake of robustness, we will set the cut-off distance for clusters recognition to 5 fm.

1. The caloric curve

Fig. 10 shows the internal energy evolution after the (asymmetric) *pasta* was well established for $x = 0.3$ [15]. The corresponding energy for the symmetric situation is included for comparison reasons.

The two profiles exhibited in Fig. 10 are very similar, regardless of the obvious overall energy bias. However, a noticeable difference can be pointed out: the sharp “jumps” observed near $T = 1$ MeV in the symmetric situation are actually not visible in the $x = 0.3$ situation.

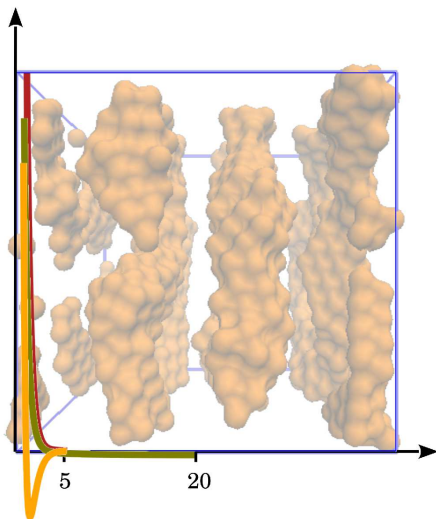


FIG. 9. (On-line color only) Potentials as a function of distance (fm). The red curve corresponds to $V_{nn}(r)$, the orange curve corresponds to $V_{np}(r)$ and the green one to $V_{pp}(r)$ (includes the Coulomb contribution). The semi-transparent image in the background represents a *lasagna*-like structure for $\rho = 0.05$ and $x = 0.3$ (only protons are represented).

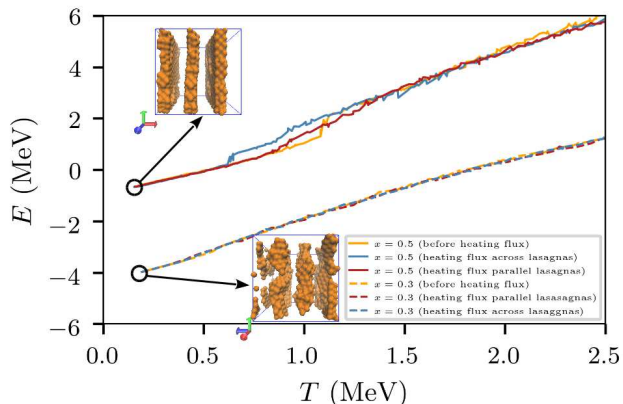


FIG. 10. (On-line color only) Internal energy vs. temperature during the heating evolution after the *pasta* was established. Two lasagna-like systems are represented ($x = 0.3$ and $x = 0.5$) for the density $\rho = 0.05$. The asymmetric situations correspond to the dashed lines, while the symmetric ones correspond to the continuous lines.

In order to get a more accurate picture of the asymmetric situation ($x = 0.3$) we computed the proton clusters along the *pasta* regime. The results are shown in Fig. 11. The cut-off distance for neighboring protons belonging to the same cluster was set to $r_c = 5$ fm.

According to Fig. 11, a few clusters exist for “cold” neutron star matter. These get gradually connected as the system is warmed, until no clusters can be

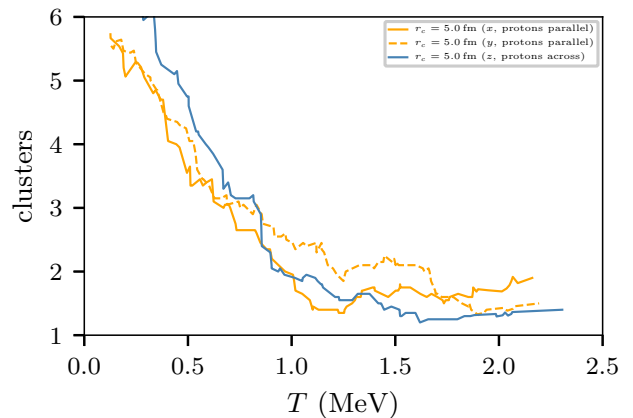


FIG. 11. (On-line color only) Number of clusters in the simulation cell for the lasagna-like structures shown in Fig. 13. Data corresponds to two heat flux: parallel or across the lasagna structure (see insert for details). The smoothing was done following a moving average procedure of ± 10 points. The cut-off distance was set to 5 fm.

distinguished at all. The connecting process appears to be fulfilled near $T = 1$ MeV (notice the vanishing slope in Fig. 11). Thus, the lack of visible energy “jumps” in Fig. 10 for the proton ratio $x = 0.3$ does not mean the absence of a *pasta* breakdown, but the embedding of this topological transition into the spread around neutrons. Fig. 12 pictures the topology transition in full colors and semi-transparent colors for $T \simeq 0.7$ MeV.

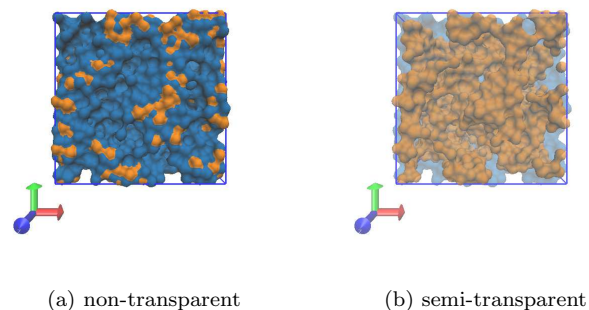


FIG. 12. Surface plots for protons (orange) and neutrons (blue) at $T = 0.7$ MeV ($\rho = 0.05$ and $x = 0.3$). The left snapshot shows a view from one side of the cell (in full colors). The right snapshot shows the same view in semi-transparent colors.

2. The thermal conductivity κ

The thermal conductivity for non-symmetric neutron star matter was computed in the same way as in Section IV A 2. Fig. 13 shows the proton thermal conductivity behavior for the $x = 0.3$ situation, evolving from “cold” (solid) temperatures to “warm” ones. The corresponding snapshots (protons only) are also exhibited.

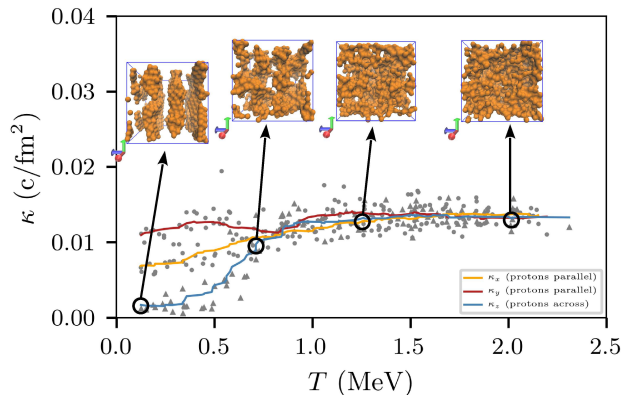


FIG. 13. (On-line color only) Proton thermal conductivity κ vs. temperature for $\rho = 0.05$ and proton ratio $x = 0.3$. The smoothing was done following a moving average procedure of ± 10 points. The rounded gray points correspond to data obtained along the lasagna direction. The triangular gray points correspond to data across the lasagna structure.

Notice that the (qualitative) patterns appearing in Fig. 13 resemble those exhibited in Fig. 5 for the symmetric situation (and for similar density). The proton conductivity across the slabs vanishes. Besides, the conductivity “decoupling” is present on either symmetric and non-symmetric matter, in correspondence with the topological transformations (*i.e.* the cluster drop-off shown in Fig. 6 and Fig. 11, respectively). The “decoupling threshold” at this instance, however, appears somewhat biased with respect to the symmetric situation.

Fig. 14 brings out the complete picture for the proton thermal conductivity κ . Although the profiles are qualitatively similar, the asymmetric proton conductivity values scale down with respect to the symmetric proton conductivity. Say, the parallel conductivity for $x = 0.3$ (see Fig. 14) never surpasses $0.01 c/fm^2$, while the corresponding values for $x = 0.5$ appear always above. Furthermore, the later reports a maximum at the solid state (“cold” temperatures), while the former does not.

The overall thermal conductivity (that is, considering *all* the nucleons) appears to be very similar for symmetric and non-symmetric matter, at “warm”

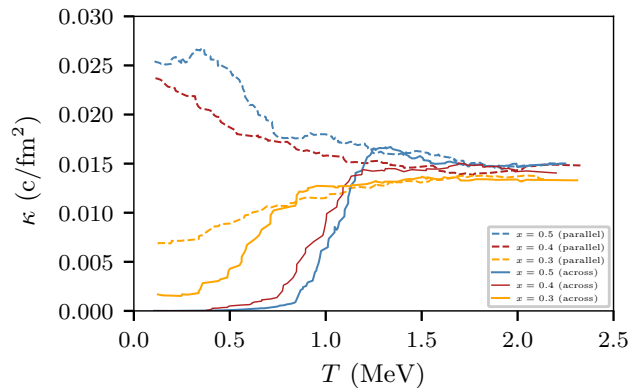


FIG. 14. (On-line color only) Proton thermal conductivity κ vs. temperature for $\rho = 0.05$ and proton ratios in the range $x = 0.3$ to 0.5 (see insert for details). The smoothing was done following a moving average procedure of ± 10 points. The dashed lines correspond to the thermal conductivity values along (parallel) the pasta structure. The continuous lines correspond to the thermal conductivity across the pasta structure.

temperatures. The corresponding profile for $x = 0.3$ is shown in Fig. 15. The neutron thermal conductivity is also included. Both profiles are remarkably similar, meaning that the thermal conduction for $x = 0.3$ is mostly achieved by neutrons.

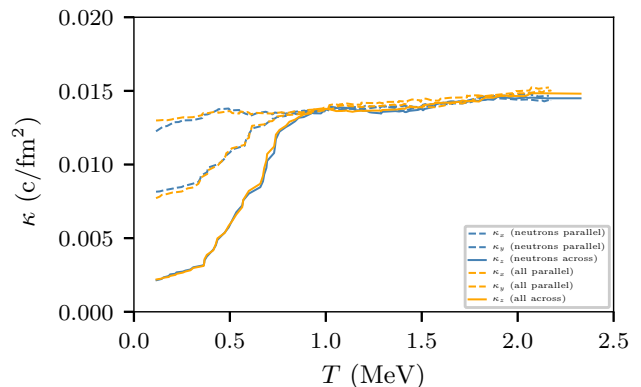


FIG. 15. (On-line color only) Thermal conductivity κ vs. temperature for $\rho = 0.05$ and proton ratio $x = 0.3$. The blue lines correspond to the neutron conductivity, while the orange lines consider *all* the nucleons (see insert for details). The dashed lines (regardless for the color) correspond to the conductivity along (parallel) the spaghetti structure. The continuous lines, instead, correspond to any direction across the spaghetti structure. The smoothing was done following a moving average procedure of ± 10 points.

The above observations indicate that the thermal conductivity for non-symmetric matter shares the same qualitative behavior as the symmetric matter, despite

that *pastas* are now embedded in a cloud of neutrons. The neutron thermal conductivity, though, resembles better the overall conductivity than the proton conductivity.

V. CONCLUSIONS

The thermal conductivity of *pastas* raises as a complex magnitude that is far from attaining a well established behavior. Researchers admit that variations of κ of (at least) an order of magnitude can be expected at sub-saturation densities, and temperatures below 2 MeV. The proton fraction is also a significant source of variations and a challenging field of investigation.

Since the *pasta* structures may become too complex for an increasing number of nucleons, we focused on simple structures (say, *lasagnas* and *spaghettis*) housing 4000 nucleons. We arrived to the main conclusion that the *pasta* breakdown process accomplishes a dramatic change of the phononic thermal conductivity. Neutron star matter switches from a strong non-isotropic regime (at the well-formed *pastas* regime) to an isotropic one, as temperature increases. This occurs sharply around $T \simeq 1$ MeV for symmetric matter, and somewhat below this threshold for non-symmetric matter.

The above conclusion is a compelling reason for associating the *pasta* topological transition to low (or high) phononic thermal conductivities, although an estimate of the “effective” κ across the neutron star crust is not yet available. The *pasta* breakdown threshold, though, appears as a key issue for this estimate.

An insight into the breakdown threshold shows the crucial role of the “connecting” nucleons between *lasagnas* or *spaghettis*. The heat flux at the threshold can only be sustained if a (small) fraction of nucleons bridge the slabs or rods. But as soon as these bridges open, the thermal conductivity (in the bridging direction) drops off. The temporary character of these connections leads to significant fluctuation of κ close to the threshold.

The phononic thermal conductivity appears “decoupled” at the well-formed *pasta* regime (say, below $T \simeq 1$ MeV for symmetric matter). The heat flux drops off across void regions, but enhances along the *pasta* structure. κ exhibits a maximum at the solid-liquid transition for symmetric matter. We may expect, therefore, that the coldest pathways in the crust become also true directions for heat conduction.

Attention was claimed in the literature on the existence of neutron-rich layers in the deep crust. The (overall) phononic thermal conductivity does not exhibit relevant variations with respect to the proton fraction at

such “warm” temperatures. The heat conduction, however, appears to be driven by the richest species. Recall that *pastas* are actually not present above $T \simeq 1$ MeV.

The “decoupling” phenomenon still appears in the well-formed *pasta* regime for neutron-rich matter. The *pastas* are actually embedded in a cloud of neutrons, seemingly isolated since the thermal conductivity drops off across the structures. Besides, the solid-liquid transition does not accomplish a conductivity enhancement, as occurs in symmetric matter. The irregularity of the slabs (due to the low proton fraction) seems to be the possible reason for this instance. We support this conclusion on the fact that the neutron thermal conductivity level for $x = 0.3$ (at the solid-liquid transition) is similar to the proton conductivity for $x = 0.5$ and $\rho = 0.03 - 0.04$. That is, both situations account for the same topological “defects”, although for two different conditions.

ACKNOWLEDGMENTS

This work was supported by the National Scientific and Technical Research Council, Argentina (spanish: Consejo Nacional de Investigaciones Científicas y Técnicas - CONICET) grant number PIP 2015-2017 GI, founding D4247(12-22-2016). AS was partially supported by U.S. National Science Foundation under contract: CBET 1404823.

-
- [1] P. Alcain and C. Dorso, Nuclear Physics A **961**, 183 (2017).
- [2] E. Flowers and N. Itoh, Astrophysical Journal - ASTROPHYS J **230**, 847 (1979).
- [3] P. S. Shternin and D. G. Yakovlev, Phys. Rev. D **75**, 103004 (2007).
- [4] R. Nandi and S. Schramm, Journal of Astrophysics and Astronomy **39**, 40 (2018).
- [5] C. O. Dorso, P. A. Giménez Molinelli, and J. A. López, Phys. Rev. C **86**, 055805 (2012).
- [6] C. Bertulani, *Neutron star crust* (Nova Science Publishers, Hauppauge, N.Y, 2011).
- [7] C. J. Horowitz and D. K. Berry, Phys. Rev. C **78**, 035806 (2008).
- [8] A. S. Schneider, D. K. Berry, M. E. Caplan, C. J. Horowitz, and Z. Lin, Phys. Rev. C **93**, 065806 (2016).
- [9] P. B. Jones, Monthly Notices of the Royal Astronomical Society **351**, 1956 (2004).
- [10] P. S. Shternin, M. Baldo, and P. Haensel, Phys. Rev. C **88**, 065803 (2013).
- [11] A. Deibel, A. Cumming, E. F. Brown, and S. Reddy, The Astrophysical Journal **839**, 95 (2017).
- [12] C. J. Horowitz, D. K. Berry, C. M. Briggs, M. E. Caplan, A. Cumming, and A. S. Schneider, Phys. Rev. Lett. **114**, 031102 (2015).
- [13] P. S. Shternin, M. Baldo, and H.-J. Schulze, Journal of Physics: Conference Series **932**, 012042 (2017).
- [14] R. Nandi and S. Schramm, The Astrophysical Journal **852**, 135 (2018).
- [15] C. Dorso, G. Frank, and J. Lpez, Nuclear Physics A (2019).
- [16] C. Dorso, G. Frank, and J. Lpez, Nuclear Physics A **978**, 35 (2018).
- [17] H. Kim, M. H. Kim, and M. Kaviany, Journal of Applied Physics **115**, 123510 (2014).
- [18] P. Kumar and H. E. Stanley, The Journal of Physical Chemistry B **115**, 14269 (2011).
- [19] J. M. Dunn, Open Access Theses - Purdue e-Pubs **766** (2016).
- [20] P. N. Alcain, P. A. Giménez Molinelli, and C. O. Dorso, Phys. Rev. C **90**, 065803 (2014).
- [21] J. A. López, E. Ramírez-Homs, R. González, and R. Ravelo, Phys. Rev. C **89**, 024611 (2014).
- [22] P. N. Alcain, P. A. Giménez Molinelli, J. I. Nichols, and C. O. Dorso, Phys. Rev. C **89**, 055801 (2014).
- [23] J. M. Dunn, J. Chem. Phys **106**, 6082 (1997).
- [24] Y. Zhou, B. Anglin, and A. Strachan, The Journal of chemical physics **127**, 184702 (2007).
- [25] J. Dunn, E. Antillon, J. Maassen, M. Lundstrom, and A. Strachan, Journal of Applied Physics **120**, 225112 (2016).
- [26] K.-H. Lin and A. Strachan, Physical Review B **87**, 115302 (2013).
- [27] S. Plimpton, Journal of Computational Physics **117**, 1 (1995).